Drag-free control of the GOCE satellite: noise and observer design

Drag-Free Control of the GOCE satellite: noise and observer design

Enrico Canuto (+), Andres Molano (+), Luca Massotti (°)

(+) Politecnico di Torino, Dipartimento di Automatica e Informatica

Corso Duca degli Abruzzi 24, 10129 Torino, Italy

enrico.canuto@polito.it, andres.molanojimenez@polito.it

(°) ESA Earth Observation Programme, Future Missions Division, ESTEC EOP-SF, Noordwijk 2200 AG, The Netherlands

luca.massotti@esa.int

Abstract

The paper concerns model and noise design relevant to Drag-Free and Attitude Control of the European satellite GOCE (Gravity field and steady-state Ocean Circulation Explorer) under different control modes. As the model must include accurate dynamics of disturbance and measurement drifts to be rejected/estimated, noise design aims to select, and to mark with the Boolean variables of the control modes, the necessary and sufficient feedback channels (noise estimator) connecting model error to noise, which are the paths through which model state variables can be updated in real-time. Noise design is applied to a generic model encompassing position and attitude control, fed by position, rate, attitude and acceleration sensors. The resulting closed-loop becomes a state predictor, providing controllable and disturbance states to drag-free and attitude control law, switching smoothly from mode to mode. Noise estimator gains are tuned to robust performance and stability by properly assigning closed-loop eigenvalues. Tuning details and simulated results illustrating the different modes are provided.

1 Introduction

1.1 Drag-free control problems

The paper aims to outline and solve the real-time estimation and control problems which are typical of drag-free satellites. To restrict the scope but not the generality, solutions and results are limited to the European GOCE satellite (Gravity field and steady-state Ocean Circulation Explorer), which has been successfully launched from Plesetks (Russia) on March 17, 2009 [1]. Drag-free satellites establish local inertial frames to reveal gravity anomalies from the distance variation between pairs of non-rotating, free-falling bodies (proof masses). Three main control problems arise: i) to make the proof-masses free-falling by canceling non-gravitational accelerations (or 'drag', hence drag-free control); ii) to keep the proof-masses non-rotating (attitude control); iii) to keep their distance within a suitable tolerance (formation control). When, as in GOCE, each proof-mass pair is mounted on a single satellite, the satellite center-of-mass (CoM) has to be made free-

falling and each proof-mass must be actively controlled to remain at a fixed distance from it. Each proof mass and position control constitute an accelerometer. The main drawback lies in the offset and drift of the accelerometers: they propagate through drag-free control, forcing position and attitude to slowly drift. In GOCE, being a single satellite, only attitude drift must be cancelled; in a drag-free formation, relative position would also need to be controlled.

1.2 Sensor fusion and noise design

The accelerometer solution looks attractive and flexible from the control standpoint, since smaller masses track a larger mass, the spacecraft. In this way, the frequency bandwidth of the accelerometer measurements can be made wider than drag-free sampling frequency (10 Hz in the GOCE case) and the noise can be made extremely small in a mid-frequency band, so as to allow for fine measurement and cancellation of non-gravitational forces. Accelerometers must be integrated with attitude/position sensors to compensate for accelerometer bias and drift. The combination of acceleration (center-of-mass and angular) and position/attitude measurements is a typical real-time sensor fusion, where the two measurements complement each other due to different bandwidths and noise. Acceleration measurements are larger bandwidth and, if doubly integrated, are less noisy at higher frequencies than are position and attitude. On the contrary, position/attitude measurements are provided at lower sampling rates (< 2 Hz) and are affected by greater noise, though the latter is bounded from DC to Nyquist frequency $f_{\max}$. Position data for low Earth orbiters, as for the GOCE, come from a Global Positioning System (GPS) receiver, whereas attitude comes from star trackers. Control requirements are expressed as piecewise spectral densities of the residual acceleration and attitude in a domain from DC to the Nyquist frequency; the domain is usually partitioned into low-, mid- and high-frequency bands as follows

$$\mathcal{F}_0 = \{ f < f_1 = 5 \text{ mHz} \},\ \mathcal{F}_1 = \{ f_1 \le f < f_2 = 0.1 \text{ Hz} \},\ \mathcal{F}_2 = \{ f_2 \le f < f_{\max} = 5 \text{ Hz} \}. \quad (1)$$

Traditionally, drag-free control is an inner loop of attitude/formation control [2]. The drag-free loop, fed by accelerometer measurements, is designed through H_∞ techniques, [3], [4], to match drag spectral density with the residual acceleration profile. The outer loop, for instance attitude, is designed via Linear Quadratic Gaussian (LQG) techniques to recover attitude rate and acceleration bias. Here a generic approach is suggested in the framework of Embedded Model Control [5]. The key is the design of the disturbance dynamics to be counteracted, which may vary because of different sensors and requirements under different control modes. Disturbance dynamics is driven by a noise vector of suitable size and location, which represents the unpredictable innovation to be real-time estimated from measurements. By selecting appropriate noise components through Boolean variables, different disturbance dynamics can be shaped and smoothly switched to different mission phases.

1.3 Overview of the paper

Section 2 shows similarities between CoM and attitude dynamics in view of a generic model. Section 3 outlines the Embedded Model construction, valid for position and attitude control and different mission phases. Noise design starts from an unobservable and reducible Embedded Model to provide a model class which is observable, irreducible-noise and decomposed between the available output measures, depending on the control mode parameterized by a Boolean vector. The result is a set of noise estimators, driven by univariate model errors, which combine with the Embedded Model to provide the state predictor. Section 4 exploits state prediction to feed a control law which guarantees performance achievement, in this case zero tracking. Robust stability and performance in the presence of neglected dynamics are then guaranteed by tuning state predictor eigenvalues to satisfy some inequalities. Tuning is then applied to pure drag-free control. Section 5 shows some simulated results of the GOCE drag-free and attitude control along with different mission phases.

2 Satellite dynamics, noise and perturbations

2.1 Reference frames

Center-of-mass and attitude dynamics are written in the spacecraft body frame $\mathcal{R}=\{C,\mathbf{i},\mathbf{j},\mathbf{k}\}$. The spacecraft is a slender cylindrical body and the cylinder axis along the direction of motion defines $\mathbf{i}$. The mean plane of the solar panels defines $\mathbf{k}$, and $\mathbf{j}$ points to the active side of the panels. Attitude control keeps the body frame aligned to the Local Orbit Reference Frame (LORF) $\mathcal{R}_O=\{C,\mathbf{i}_O,\mathbf{j}_O,\mathbf{k}_O\}$, defined by the Earth-centered position $\mathbf{r}$ and the velocity $\mathbf{v}$ of the spacecraft center-of-mass, as follows

$$\mathbf{i}_O=\mathbf{v}/|\mathbf{v}|,\ \mathbf{j}_O=\mathbf{r}\times\mathbf{v}/|\mathbf{r}\times\mathbf{v}|,\ \ \mathbf{k}_O=\mathbf{i}_O\times\mathbf{j}_O. \tag{2}$$

Due to the a small orbit eccentricity, $\mathbf{r}$ and $\mathbf{v}$ are not orthogonal and $\mathbf{k}$ is slightly misaligned from $\mathbf{r}$. The body-to-LORF transformation $R(\mathbf{q})$ defines the attitude $\mathbf{q}^T=\begin{bmatrix}q_x & q_y & q_z\end{bmatrix}$ as a vector of small Euler rotations in agreement with the fine attitude control treated here. A third frame $\underline{\mathcal{R}}=\{C_E,\underline{\mathbf{i}},\underline{\mathbf{j}},\underline{\mathbf{k}}\}$, centered on the Earth's CoM C_E, defines the reference circular orbit of radius $\underline{r}$ and angular rate $\underline{\omega}$. The unit vector $\underline{\mathbf{i}}$ is tangential and motion-directed, $\underline{\mathbf{j}}$ is inertial and normal to the orbit plane, and $\underline{\mathbf{k}}$, radial, points to the satellite. The perturbed satellite position $\mathbf{r}$ can thus be resolved into the sum

$$\mathbf{r}=\underline{\mathbf{r}}+\Delta\mathbf{r}=\underline{r}\underline{\mathbf{k}}+\Delta x\underline{\mathbf{i}}+\Delta y\underline{\mathbf{j}}+\Delta z\underline{\mathbf{k}}, \tag{3}$$

where $|\Delta\mathbf{r}|$ is much less than $\underline{r}$, close to the eccentricity fraction, over time intervals lasting tens of orbital periods. The perturbation $\Delta\mathbf{r}$ is due to anomalies in the Earth's gravity and to residual drag. When reference and actual orbits are slightly apart, the LORF-to-reference transformation $R_O(\mathbf{q}_O)$ defines the LORF attitude

$$\mathbf{q}_O^T=\begin{bmatrix}-\Delta y/\underline{r} & \Delta x/\underline{r}-\Delta\dot{z}/(\underline{\omega}\underline{r}) & \Delta\dot{y}/(\underline{\omega}\underline{r})\end{bmatrix}, \tag{4}$$

which provides monitoring of reference and actual orbit discrepancy.

2.2 Perturbed CoM and attitude dynamics

Let the rates of the perturbed CoM position and velocity, in the reference frame, be denoted with $\dot{\Delta\mathbf{r}}$ and $\dot{\Delta\mathbf{v}}$. Then, under small $\mathbf{q}_O$, the following relative dynamics hold

$$\begin{aligned}\dot{\Delta\mathbf{r}} &= \Delta\mathbf{v}\\ \dot{\Delta\mathbf{v}} &= -\underline{\boldsymbol{\omega}}\times\left(\underline{\boldsymbol{\omega}}\times\underline{\mathbf{r}}+\underline{\boldsymbol{\omega}}\times\Delta\mathbf{r}+2\Delta\mathbf{v}\right)-\nabla U\left(\underline{\mathbf{r}}\right)-\nabla^2 U\left(\underline{\mathbf{r}}\right)\Delta\mathbf{r}+R_O\left(\mathbf{q}_O\right)R\left(\mathbf{q}\right)\left(\mathbf{D}+\mathbf{F}\right)/m_s\end{aligned}, \tag{5}$$

where $\underline{\boldsymbol{\omega}}=\underline{\omega}\,\underline{\mathbf{j}}$ is the reference orbital rate, gravity acceleration derives from a quadratic expansion of the gravity potential U, $\mathbf{D}$ and $\mathbf{F}$ denote drag and command forces in body coordinates, and m_s the spacecraft mass. Equation (5) simplifies to the classical Hill's equation [6] if spherical gravity terms are made explicit. Moreover, assuming small attitude $\mathbf{q}$ and neglecting second order terms, equation (5), valid also in body coordinates, simplifies to

$$\dot{\Delta\mathbf{r}}=\Delta\mathbf{v},\ \dot{\Delta\mathbf{v}}=-2Z\underline{\omega}\Delta\mathbf{v}-\underline{\omega}^2K^2\Delta\mathbf{r}-\Delta\mathbf{g}\left(\underline{\mathbf{r}},\Delta\mathbf{r}\right)+\left(\mathbf{D}+\mathbf{F}\right)/m_s, \tag{6}$$

where the matrices

$$Z=\begin{bmatrix}0&0&1\\0&0&0\\-1&0&0\end{bmatrix},\ K=\begin{bmatrix}0&0&0\\0&1&0\\0&0&j\sqrt{3}\end{bmatrix} \tag{7}$$

make spherical gravity terms explicit and $\Delta\mathbf{g}\left(\underline{\mathbf{r}},\Delta\mathbf{r}\right)$ accounts for gravity anomalies. Interestingly, a similar equation applies to small attitude angles, upon definition of the angular rate $\boldsymbol{\omega}$ in body coordinates and of the LORF-to-body rate error $\Delta\boldsymbol{\omega}=\boldsymbol{\omega}-R^T\left(\mathbf{q}\right)\underline{\omega}\mathbf{j}$; it holds

$$\dot{\mathbf{q}}=\Delta\boldsymbol{\omega},\ \dot{\Delta\boldsymbol{\omega}}=-2Z_q\underline{\omega}\Delta\boldsymbol{\omega}-\underline{\omega}^2K_q^2\mathbf{q}+J_s^{-1}\left(\mathbf{D}_q+\mathbf{C}\right). \tag{8}$$

The first term on the right-hand side is the linearized gyro-acceleration, the second term is the linearized gravity-gradient acceleration; the last two terms, $\mathbf{D}_q$ and $\mathbf{C}$, denote environmental perturbations (aerodynamic and magnetic) and commanded torques. The GOCE inertia tensor J_s is quasi diagonal, but largely unbalanced, i.e. $J_{sx}<<J_{sy}\simeq J_{sz}$, due to the spacecraft's shape, which leads to the gyro term in (8). The first two matrices may be approximated as

$$Z_q\simeq\begin{bmatrix}0&0&-1/8\\0&0&0\\1/2&0&0\end{bmatrix},\ K_q\simeq\begin{bmatrix}<1&0&0\\0&j\sqrt{3}&0\\0&0&0\end{bmatrix}, \tag{9}$$

the values depending on the inertia tensor. Equations (6) and (8) must be completed with sensor/actuator noise as well as perturbation dynamics before passing to the Embedded Model and noise design.

2.3 Perturbing forces and torques

Three perturbations significantly affect position and attitude dynamics at a low Earth orbit: (i) aspherical gravity anomalies $\Delta\mathbf{g}\left(\underline{\mathbf{r}},\Delta\mathbf{r}\right)$, (ii) aerodynamic forces and torques due to thermosphere and wind; (iii) magnetic torque due to coupling of the Earth's magnetic field with the spacecraft's

magnetic dipole moment. Aerodynamic forces are the most significant at low Earth orbit. Although their time-profile is periodic with the orbital rate, it must be held to be highly uncertain and unpredictable, both in the short and in the longer term. In the short term, they can only be modeled by non-stationary stochastic processes. Noise design does not require accurate models, but requires knowledge of the spectral shape up to the control Nyquist frequency $f_{\max}$. To this end, long-term models have been combined with short-term ones and stochastically interpolated. As a result, drag spectral density is enveloped by first- to second-order drifts in the mission bandwidth $\mathcal{F}_1$. Since the same shape applies to gravity anomalies, the spectral density of perturbing forces is assumed to be enveloped as follows

$$S_d^2(f) \le S_{d0}^2 \left(1+\left(f / f_{d1}\right)^2\right)^{-1} \left(1+\left(f / f_{d2}\right)^2\right)^{-1}, \tag{10}$$

where $f_{d1} < f_1$, and $f_{d2} < f_2$. Perturbing torques are a combination of aerodynamic and magnetic effects. Under attitude control, aerodynamic torques may become smaller than magnetic torques. The latter may be contrasted by simple magnetic torquers, which implies that the residual torques share a spectral profile as in (10).

2.4 Sensor/actuator noise and dynamics

2.4.1 Accelerometer

Only accelerometer noise is treated, being specific to drag-free control. The servo-accelerometer measure y_a is equal to the restoring acceleration a plus a disturbance d_a. Within the accelerometer bandwidth $f_a \simeq 20$ Hz, d_a is the combination of the position-sensor noise w_{ay} and of the command disturbance; the latter may be partitioned into drift (including bias b_a) and white noise w_{a0}, as follows

$$\begin{aligned} y_a(f) &= a(f) + d_a(f) \\ d_a(f) &= \left(j2\pi f\right)^{-1} w_{a1}(f) + w_{a0}(f) - \left(f / f_a\right)^2 w_{ay}(f) \end{aligned}. \tag{11}$$

Then, assuming statistical independence and factoring out the flat spectral density S_{u0}^2 of w_{a0}, the spectral density of the total noise d_a may be expressed in a compact form by

$$S_a^2(f) = \left(\left(f_u / f\right)^{2s} + 1 + \left(f / f_h\right)^4\right) S_{a0}^2, \; s = 1 \div 2. \tag{12}$$

Assuming $f_u < f_1$ and $f_h > f_2$ in (12) implies that $S_a(f)$ is minimal across the mission band $\mathcal{F}_1$. The bowl-shape resulting from (12) is typical of servo-accelerometers; the second derivative of the sensor noise w_{ay} shapes the high-frequency rim, referred to as f^2 noise; actuator noise and drift shape the low-frequency side. Accelerometer servo-dynamics may be neglected if $f_{\max} < f_a$. Accelerometer measurements must be anti-aliased to avoid folding of the f^2 noise across $f_{\max}$. Anti-aliasing and transmission delays are treated in the Embedded Model as a first-order plus neglected dynamics.

2.4.2 Electric propulsion

GOCE will employ proportional electric mini-thrusters to counteract the along-track drag. In addition, the first GOCE design relied on electric micro-thrusters, for cross-track drag-free and attitude control. Micro-propulsion technology not being mature, it was abandoned in favor of traditional magnetic control, which is only restricted to attitude. Since then, micro-thrusting has evolved and will be one of the key technologies for future scientific missions. This justifies assuming micro-propulsion in the present analysis. The dynamics of electrostatic thrusters is a combination of propellant flow and ionization. Since PID regulators are employed, second order dynamics between voltage command u and thrust F applies, with a resonance frequency $f_t > f_{\max}$. By restricting the frequency band to $f < f_t$, the thruster noise spectral density can be written as

$$S_t^2(f) = \left(\left(f_l / f \right)^{2r} + 1 \right) S_{t0}^2, \tag{13}$$

where $f_l < f_{\max}$ may be anywhere within the mission band $\mathcal{F}_1$. Different thruster configurations are possible. The first GOCE design assumed that a single mini-thruster was used to counteract the along-track drag, and $m = 8$ micro-thrusters to actuate lateral, angular drag-free as well as attitude control. By neglecting thruster dynamics, the static voltage to force/torque relation can be written as

$$\begin{bmatrix} \mathbf{F} \\ \mathbf{C} \end{bmatrix}(t) = \begin{bmatrix} B \\ B_q \end{bmatrix} \left(\mathbf{u}(t) + \mathbf{w}_t(t) \right), \tag{14}$$

where $\mathbf{u} \geq 0$ is the thrust command vector, and $\mathbf{w}_t$ denotes the overall noise defined in (13). $\mathbf{F}$ and $\mathbf{C}$ have been defined in (6) and (8). The thrust distribution matrices B and B_q, converting $\mathbf{u}$ into forces and torques, mainly depend on the thruster geometry.

3 Embedded model and noise design

3.1 Introduction

Embedded Model Control [5] aims to exactly replicate the design model within control algorithms. To this end, disturbance spectral densities like (10), (12) and (13) are not converted to weighting functions [7], but to simple stochastic equations to be real-time updated by the estimated innovation [8]. Observable though unpredictable disturbances can thus be explicitly rejected in a timely manner by the control law.

3.2 Controllable dynamics and output equation

Exploiting the similarity of (6) and (8), and coordinate decomposition, a unique class of Embedded Models can be derived. Coordinate decomposition follows assuming damping and harmonic coupling terms in (6) and (8) to be weak with respect to closed-loop eigenvalues, which is true when $(2\pi)\omega << f_{\max} = 0.5/T$, where $T = 0.1$ s is the designed control time unit. That leads to splitting (6) and (8) into six independent discrete-time state equations, only connected by known perturbations and the thrust distribution matrices in (14). By denoting a component of $\Delta\mathbf{r}$ and $\mathbf{q}$

with x_c, and a component of $\Delta\mathbf{v}T$ and $\Delta\boldsymbol{\omega}T$ with v_c, the generic single-axis dynamics can be written as

$$\begin{aligned}&\mathbf{x}_c(i+1)=A_c\mathbf{x}_c(i)+B_c\left(\left(1-l_v(i)\right)\underline{g}(i)+d_g(i)+a(i)\right),\ a(i)=d_d(i)+l_v(i)\underline{d}(i)+B_u\mathbf{u}(i)\\&\mathbf{x}_c=\begin{bmatrix}x_c\\v_c\end{bmatrix},\ A_c=\begin{bmatrix}1&1\\0&1\end{bmatrix},\ B_c=\begin{bmatrix}0\\T^2\end{bmatrix}\end{aligned}\quad . \tag{15}$$

In (15), $\underline{g}$ is the known gravity term from (6) which has been separated from $\underline{d}$, since only the latter, expressing known gyro and gravity-gradient terms in (8), must be cancelled. To represent both of them in (15), the Boolean variable $l_v=\{0,1\}$ has been added, switching from position (=0) to attitude (=1). The term d_g encompasses unknown gravity terms and, in drag-free satellites, it also includes accelerometer bias and drift; d_d includes non-gravitational forces from (6) and torques from (8) that are to be cancelled; a is the residual drag-free acceleration free of accelerometer drift and bias, and B_u is a matrix row in (14). Thruster noise from (14) is included in d_d.

Equation (15) must be completed with the disturbance dynamics (Section 3.3) and the position, rate, and acceleration output equations (see Section 2.4):

$$\begin{aligned}&z_a(i+1)=\left(1-\beta_a\right)z_a(i)+\beta_a\left(a(i)+d_a(i)\right)\\&\mathbf{y}(i)=\begin{bmatrix}y_c\\y_v\\y_a\end{bmatrix}(i)=C(i)\begin{bmatrix}\mathbf{x}_c\\z_a\end{bmatrix}(i)+\mathbf{e}(i),\ C(i)=\begin{bmatrix}1&0&0\\0&1-l_v(i)&0\\0&0&l_a(i)\end{bmatrix}.\end{aligned}\tag{16}$$

In (16), $l_a=\{0,1\}$ is a Boolean variable switching the accelerometer ON/OFF; z_a is the state of the modeled dynamics from thruster to accelerometer, where $\beta\simeq 1$; d_a is the overall accelerometer noise defined in (11), and $\dim\mathbf{y}=n_y$. Accelerometer switching occurs in time, at different mission phases. Rate measurements are only employed ($l_v=0$) for position estimation (GOCE), because GPS rate data are so accurate that they greatly improve noise estimates with respect to position alone. The opposite occurs with star trackers, which justifies ignoring rate data ($l_v=1$) in the absence of gyro measurements. In (16) $\mathbf{e}^T=\begin{bmatrix}e_c & e_v & e_a\end{bmatrix}$ is the vector of the model errors, where each component e_j, $j=a,v,c$, includes the measurement error v_j and the neglected dynamics $\partial\mathbf{P}_j$ as follows

$$e_j(z)=\partial\mathbf{P}_j(z)x_j(z)+v_j(z). \tag{17}$$

In (17), $\partial\mathbf{P}_j$ is not part of the Embedded Model, but must be explicitly given so as to select closed-loop eigenvalues which guarantee robust stability (Section 4.2). For instance, $\partial\mathbf{P}_a$ expresses the fractional error of the thruster-to-accelerometer dynamics (Sections 2.4.1 and 2.4.2, [1], [9]) with respect to the 1st order dynamics (16).

3.3 Disturbance dynamics

Disturbance dynamics is the first step in noise design. Each of the unknown perturbations in (15) and (16), namely d_k, $k = g,d,a$, is assumed be a composition of white noise, first- and second-order drift as follows

$$\begin{aligned} &\mathbf{x}_k(i+1) = A_k\mathbf{x}_k(i) + G_k\mathbf{w}_k(i), \\ &d_k(i) = C_k\mathbf{x}_k(i) + H_k\mathbf{w}_k(i) \\ &\mathbf{x}_k^T = \begin{bmatrix} x_k & v_k \end{bmatrix},\ \mathbf{w}_k^T = \begin{bmatrix} w_{0k} & w_{1k} & w_{2k} \end{bmatrix} \end{aligned} \quad . \tag{18}$$

That is consistent with (10), (12) and (13), except for the f^2 noise in (12), which is simplified to a white noise, being significant only close to $f_{\max}$. The detail of matrices in (18) is as follows

$$\left[\begin{array}{c|c} A_k & G_k \\ \hline C_k & H_k \end{array}\right] = \left[\begin{array}{cc|ccc} 1 & 1 & 0 & 1 & 0 \\ 0 & 1 & 0 & 0 & 1 \\ \hline 1 & 0 & 1 & 0 & 0 \end{array}\right]. \tag{19}$$

3.4 The Embedded Model

The equations (15), (16) and (18) define the Embedded Model, driven by $\mathbf{u}$ and the noise vector $\mathbf{w}^T = \begin{bmatrix} \mathbf{w}_g^T & \mathbf{w}_d^T & \mathbf{w}_a^T \end{bmatrix}$ of size n_w, and having state $\mathbf{x}^T = \begin{bmatrix} \mathbf{x}_c^T & z_a & \mathbf{x}_g^T & \mathbf{x}_d^T & \mathbf{x}_a^T \end{bmatrix}$ of size n. The model is made variable by a Boolean vector $\mathbf{l}^T = \begin{bmatrix} l_v & l_a & l_g \end{bmatrix}$, where l_g is defined in Section 3.5. Noise is assumed to be a class of bounded, arbitrary signals where no causal relation exists between $\mathbf{w}(i)$ and the past $\mathbf{w}(i-h)$, $h>0$. The best prediction of $\mathbf{w}(i)$ from the past is fixed to zero. The model of a single axis may be written in the compact form

$$\begin{aligned} &\mathbf{x}(i+1) = A\mathbf{x}(i) + B\mathbf{u} + \underline{\mathbf{d}}\left(\mathbf{l}(i), i\right) + G\left(\mathbf{l}(i)\right)\mathbf{w}(i) \\ &\mathbf{y}(i) = C\left(\mathbf{l}(i)\right)\mathbf{x}(i) + \mathbf{e}(i) = \mathbf{y}_m(i) + \mathbf{e}(i) \end{aligned} \quad , \tag{20}$$

the known disturbance components from (15) having been merged into the vector $\underline{\mathbf{d}}$ and the model output denoted with $\mathbf{y}_m$. By reordering the state vector $\mathbf{x}$, the matrix G, $n \times n_w$, in (20) can be transformed into

$$G = \begin{bmatrix} G_0 & G_0H \\ JG_0 & JG_0H \end{bmatrix}, \tag{21}$$

where G_0, $m_w \times m_w$, $m_w \le n_w$, is invertible.

3.5 Observability and noise design

The problem addressed here is to transform (20) into a state predictor, fed by $\mathbf{e}$ and $\mathbf{u}$, which is variable with $\mathbf{l}$, and bounded-input-bounded-output (BIBO) stable. A first objective requires the stabilizing feedback (called the noise estimator), which is fed by $\mathbf{e}$, to pass only through $\mathbf{w}$ and to be irreducible. A second objective concerns stability, which must be guaranteed even if the pair $\left(C(\mathbf{l}), A\right)$ is not observable.

Consider the first objective. A noise vector $\mathbf{w}_i$ is said to be irreducible when each component forces a single state variable and the pair $\left(A, G_i\right)$ is controllable; in which case $\dim G_i = n \times m_w$,

with $m_w \le n$, each column of G_i has a single nonzero element and G_i is full rank. Then, assuming (C, A) to be observable, at least one (not necessarily static) feedback from $\mathbf{e}$ to $\mathbf{w}$ exists which stabilizes the state predictor. Note the full-rank of G_i is not necessary to guarantee stability, but it simplifies feedback construction. Given G in (21), the following transformation provides G_i and $\mathbf{w}_i$:

$$\begin{aligned} \begin{bmatrix} G_i & 0 \end{bmatrix} &= \begin{bmatrix} I & 0 \\ 0 & 0 \end{bmatrix} = \begin{bmatrix} I & 0 \\ -J & I \end{bmatrix} \begin{bmatrix} G_0 & G_0 H \\ JG_0 & JG_0 H \end{bmatrix} \begin{bmatrix} G_0^{-1} & -H \\ 0 & I \end{bmatrix}. \\ \mathbf{w}_i &= \begin{bmatrix} G_0 & G_0 H \end{bmatrix} \mathbf{w} \end{aligned} \tag{22}$$

In our case $J = 0$ and only two rows of G must be reduced as follows

$$\begin{aligned} w_{di} &= w_{d0} + w_{g0} \\ w_{ai} &= \beta_a \left(w_{d0} + w_{a0} \right) \end{aligned}. \tag{23}$$

Noise statistics and correlation change under (22), which may reflect on feedback design. Here components in (23) are assumed to be retrieved from different measurements.

The next step is an irreducible noise estimator, i.e. when each noise component is fed by the least number of measurements (in the limit case, one) and the feedback dynamic is of least order (in the limit case, zero). Here we restrict the analysis to the form of the matrices in (20), where the pair (C, A) can be reordered to be block upper-triangular with n_y pairs of diagonal blocks (C_j, A_j) which are paralleled by the diagonal blocks G_{ij} in the irreducible G_i. Since n_y is the output size in (16), a univariate decomposition, such as each block is associated to a single measure, is a candidate for irreducibility. However, a necessary and sufficient condition [10] for the existence of a stabilizing feedback (not necessarily static) is that each pair (C_j, A_j) is observable and each pair (A_j, G_{ij}) is controllable. Although the latter condition may be not satisfied by a univariate decomposition – a case occurring here (Section 3.6.1)-, stability conditions may be recovered by associating each block with more than one measurement, thus leading to a multivariate decomposition.

Assuming a stabilizing feedback exists, the aim is to find the least order. Denote the relevant output, irreducible noise and model error with $y_{mj}, \mathbf{w}_{ij}, e_j$ and the noise-to-output transfer function as

$$y_{mj}(z) = \varphi_j^{-1}(z) \mathbf{M}_j^T(z) \mathbf{w}_{ij}(z), \tag{24}$$

where, by previous assumptions, no pole-zero cancellation occurs. Then denote the greatest degree of $\mathbf{M}_j(z)$ with $\deg \mathbf{M}_j(z)$, and the model-error to noise feedback with

$$\mathbf{w}_{ij}(z) = \mathbf{L}_j(z) e_j(z) = \psi_j^{-1}(z) \mathbf{N}_j(z) e_j(z), \tag{25}$$

where $\deg \mathbf{N}_j(z) = \deg \psi_j(z)$ in order for the noise estimator to be all-pass. If $\dim A_j = \dim \mathbf{w}_{ij} = n_j$, $\deg \mathbf{M}_j(z) = n_j - 1$, a static feedback $\mathbf{w}_j = \mathbf{L}_j e_j$, with $\deg \mathbf{L}_j(z) = 0$, is sufficient to stabilize the closed-loop polynomial $\varphi_j(z) + \mathbf{M}_j^T(z) \mathbf{L}_j$. If $\dim A_j > \dim \mathbf{w}_{ij} = n_{wj}$, a

sufficient condition to recover stability is $\deg\psi_j(z) \geq n_j - n_{wj}$. Note, in the latter case, both the gains of $\mathbf{N}_j(z)$ and the free coefficients of the monic $\psi_j(z)$ must be fixed by the selected closed-loop eigenvalues.

The second objective can only be met by dropping unobservable states. Actually a generic procedure is adopted: a Boolean vector $\mathbf{l}(i)$ is defined, switching OFF the noise components which drive unobservable state variables, and leaving their free response to depend on initial states to be calibrated or set to zero. Note the free-response must be bounded to ensure the required BIBO stability. A smooth switching among different models may require suitable calibration phases (Section 3.6.2). Consider for instance the addition of d_g and d_d in (15), and of their state vectors $\mathbf{x}_g$ and $\mathbf{x}_d$ through (18): they cannot be observable under $l_a = 0$, which requires a Boolean variable l_g switching $\mathbf{w}_g$ ON and OFF. The same holds for $\mathbf{x}_d$ and $\mathbf{x}_a$ when $l_a = 1$.

3.6 Noise design application

3.6.1 Center-of-mass dynamics

This case, corresponding to $l_v = 1$ in (16), does not admit of a univariate decomposition because of the rate measurement y_v. Let us restrict considerations to accelerometer ON, namely to $l_a = 1$, and assume the drag d_d to be estimated from the accelerometer, which in turn allows d_g to be estimated from rate and position, and implies $l_g = 1$. Observability is guaranteed if $\mathbf{w}_a$ is switched OFF through $1 - l_a$, in other words if $\mathbf{x}_a$ in (18) only admits of a free response, which implies the accelerometer bias has been calibrated. Consider the univariate decomposition in Table 1: it cannot lead to noise estimation since x_c is uncontrollable by noise. The reason is that no disturbance exists in (15) which directly forces x_c, since the center-of-mass position must be the output of the velocity integration, free of any perturbation. To make x_c controllable, subsets 1 and 2 in Table 1 must be merged, thus leading to a multivariate noise estimation. In the GOCE satellite, subsets 1 and 2 in Table 1 are employed to estimate the LORF as defined in (2); no orbit control is needed. Subset 3 is employed to estimate the non-gravitational forces and to drive the CoM drag-free control. The corresponding noise estimator (25) is static and reduces to

$$\psi_a(z) = 1,\ N_a(z) = L_a,\ L_a^T = \begin{bmatrix} l_{a0} & l_{a1} & l_{a2} \end{bmatrix}. \tag{26}$$

Table 1. Univariate decomposition of the CoM dynamics

Subset (subscript j)	Measure	Observable	Unobservable	Uncontrollable	Noise
1 (c)	y_c	x_c	None	x_c	None
2 (v)	y_v	v_c, $\mathbf{x}_g$	None	None	w_{1g}, w_{2g}, w_{0d}
3 (a)	y_a	z_a, $\mathbf{x}_d$	$\mathbf{x}_a$	None	w_{1d}, w_{2d}, w_{0a}

3.6.2 Attitude dynamics

Neglecting attitude rate measurements, i.e. assuming $l_v = 0$, univariate decomposition always exists whatever the values of l_d and l_a, but it may not be unique depending on which state variables have been declared unobservable. To this end, three control modes are considered, valid also for position dynamics: (i) fine pointing, when only attitude measurements are available, i.e. $l_a = 0$, which in turn implies $l_g = 0$; (ii) calibration, when accelerometer bias is calibrated, i.e. $l_a = 1$, and $l_g = 0$ is kept, since perturbation torques are still estimated from the star tracker; (iii) science, when $l_a = 1$ and $l_g = 1$, since perturbation torques are now recovered from the accelerometers.

Control modes and subsets are shown in Table 2. Restricting considerations to the science mode, subset 2 gives rise to a static noise estimator as in (26); on the contrary, subset 1 needs a dynamic estimator, since $n_1 = 4,\ n_{w1} = 3$.

Table 2. Attitude decomposition for different control modes

Control mode	Subset (subscript j)	Measure	Observable	Unobservable	Noise
Fine pointing	1 (c)	y_c	$\mathbf{x}_c, \mathbf{x}_d$	$\mathbf{x}_g$	w_{0d}, w_{1d}, w_{2d}
Calibration	1 (a)	y_c	$\mathbf{x}_c, \mathbf{x}_d$	$\mathbf{x}_g$	w_{0d}, w_{1d}, w_{2d}
	2 (c)	y_a	$z_a, \mathbf{x}_a$		$\mathbf{w}_a$
Science	1 (c)	y_c	$\mathbf{x}_c, \mathbf{x}_g$		w_{0d}, w_{1g}, w_{2g}
	2 (a)	y_a	$z_a, \mathbf{x}_d$	$\mathbf{x}_a$	w_{0a}, w_{1d}, w_{2d}

4 Embedded Model Control and eigenvalue tuning

4.1 Requirements and control law

The state predictor, which consists of the state equation (20) and of the noise estimators (25) converted to state equations, is the core of the control unit and solves the problem of real-time updating unknown disturbance dynamics. Here zero-tracking is assumed, which for the GOCE satellite amounts to the following performance equalities

$$\begin{aligned} &\mathbf{a}(t) = m_s^{-1}\left(\mathbf{D}(t) + \mathbf{F}(t)\right) = 0 \\ &\mathbf{q}(t) = 0,\ \Delta\boldsymbol{\omega}(t) = 0,\ \Delta\dot{\boldsymbol{\omega}}(t) = 0 \end{aligned} \quad . \tag{27}$$

The first equality requires zero CoM non-gravitational accelerations **a** (drag-free), the second requires zero attitude, zero angular rate and zero acceleration. Actually, in the case of GOCE, (27) must be replaced by a piecewise profile, usually bowl-shaped, which bounds the spectral density of the performance variables in the frequency bands defined in (1).

Let us restrict considerations to the science mode, namely to $l_a = 1$, $l_g = 1$ and to position drag-free control; attitude control has been partly treated in [9]. Performance variables in (27) are

converted into single-axis variables of the Embedded Model with the help of (15) and by replacing subscripts c,u with q in the attitude variables, which yields

$$\begin{aligned} &a(i) = d_d(i) + B_u\mathbf{u}(i) = 0,\ l_v = 0 \\ &x_q(i) = 0,\ v_q(i) = 0,\ a_q(i) = d_g(i) + d_d(i) + \underline{d}(i) + B_q\mathbf{u}(i) = 0,\ l_v = 1 \end{aligned}. \tag{28}$$

Drag-free and attitude control laws, which are model-based, follow immediately from (28) and the state predictor (20) and (25), by replacing unknown perturbations, say d_d, with their state variable, say x_d:

$$\begin{aligned} &B_u\mathbf{u}(i) = -d_d(i) = -x_d(i) \\ &B_q\mathbf{u}(i) = -k_x x_q(i) - k_v v_q(i) - x_g(i) - x_q(i) - \underline{d}(i) \end{aligned}. \tag{29}$$

Note that control law does not explicitly depend on the Boolean $\mathbf{l}$, as the latter only switches noise. Only the gain values may depend on it, because of different requirements in Section 5. Attitude control in (29), which is always ON from pointing to science mode, combines attitude, rate and acceleration targets in (28) through the feedback gains k_x and k_v, which ensure closed-loop stability of the controllable dynamics (15). By replicating (29) three times, six force/torque components are computed to be apportioned among $m+1=9$ thrusters, as mentioned in Section 2.4.2.

4.2 Closed-loop stability

The control law (29) and the state predictor, defined by (20) and (25), are the core of control algorithms. The control gains to be tuned are split between state feedback gains in (29) and noise estimator gains in (25). They must be tuned to guarantee stability in the presence of de-stabilizing model error components. To this end, model error e_j has been split in (17) into noise v_j, not affecting stability, and neglected dynamics $\partial\mathbf{P}_j$.

The robust stability in the presence of unstructured uncertainties is usually guaranteed in the frequency domain (H_∞ or related techniques [11]). The Embedded Model Control, as shown in [5] and applied here, provides a simple and explicit relation from $\partial\mathbf{P}_j$ to performance variables. To this end, restricting considerations to a (center-of-mass) and x_q (attitude) in (28) and following [5], the Z-transform equalities become

$$\begin{aligned} &a = \mathbf{V}_a\left(\mathbf{M}_a^{-1}e_a + d_a\right) + \mathbf{S}_a d_d \\ &x_q = -\mathbf{V}_q e_q + \mathbf{S}_q\mathbf{M}_q\left(d_g - \mathbf{V}_a\left(\mathbf{M}_a^{-1}e_a + d_a\right) + \mathbf{S}_a d_d\right) \end{aligned}, \tag{30}$$

where the controllable dynamics in (15) and (16) correspond to $\mathbf{M}_q = (z-1)^{-2}T$ and $\mathbf{M}_a = (z-1-\beta_a)^{-1}\beta_a$, respectively. In (30), $\mathbf{S}_a$ and $\mathbf{S}_q$ are the closed-loop sensitivities, whereas $\mathbf{V}_a = 1-\mathbf{S}_a$ and $\mathbf{V}_q = 1-\mathbf{S}_q$ are their complements. By replacing (17) in (30), the final expression, restricted to position drag-free control, holds:

$$\left(1+\mathbf{V}_a\partial\mathbf{P}_a\right)a = \mathbf{V}_a\left(\mathbf{M}_a^{-1}v_a + d_a\right) + \mathbf{S}_a d_d, \tag{31}$$

showing a combination of Embedded Model, neglected dynamics and state predictor.

4.3 Stability and performance inequalities

Following [5], stability and performance are ensured by tuning noise estimator gain to respect the following inequalities valid for $|f| \le f_{\max}$:

$$\begin{aligned} &\max_{|f|\le f_{\max}} |\mathbf{V}_a(f)||\partial\mathbf{P}_a(f)| \le \eta < 1 \\ &\sqrt{|\mathbf{V}_a(f)|^2 S_a^2(f) + |\mathbf{S}_a(f)|^2 S_d^2(f)} \le \bar{S}_a^2(1+\eta) \end{aligned}, \tag{32}$$

where η is the degree of robustness and $\bar{S}_a(f)$ is the upper bound to the spectral density of the residual CoM acceleration a. Inequality (32) is a rather complex expression of the gain L_a in (26), but it can be solved analytically under the following assumptions.

State-predictor eigenvalues are equal to $|\lambda_{ak} = 1-\gamma_a| < 1,\ k = 1,...,n_{aw} = 3$, and correspond to the frequency $f_a = (2\pi T)^{-1}\gamma_a$.

The highest peak of $|\partial\mathbf{P}_a(f)|$ occurs at $f_{\partial a} > f_a \in \mathcal{F}_2$, implying that $|\mathbf{V}_a(f_a)|$ is approximated by the high-frequency asymptote [5], [12], as follows

$$\mathbf{V}_{a\infty}(f) \simeq 2(2\pi fT)^{-2}\beta_a\gamma_a(1+0.5\gamma_a/\beta_a),\ f_a < f < f_{\max}. \tag{33}$$

Accelerometer and drag spectral densities S_a and S_d can be enveloped by piecewise profiles according to frequency partition (1), which enables the performance inequality in (32) to be split into three parts. To this end, (33) must be completed with the following low- and high-frequency asymptotes

$$\begin{aligned} &\mathbf{V}_{a0}(f) \simeq 1,\ \mathbf{S}_{a0}(f) \simeq (2\pi fT)^2\gamma_a^{-2}(1+2\gamma_a),\ f \le f_2 < f_a \\ &\mathbf{S}_{a\infty}(f) \simeq 1,\ f > f_a \end{aligned}. \tag{34}$$

Employing (33) and (34), and replacing S_a, S_d and S_t with their asymptotes obtained from (10), (12) and (13), the pair of inequalities in (32) is converted to a single stability inequality and to three performance bounds, partitioned from $\mathcal{F}_2$ to $\mathcal{F}_0$, as follows.

$$\begin{aligned} &2\alpha_\eta\beta_a\gamma_a(1+\gamma_a\beta_a^{-1}/2) \le \eta < \eta_{\max} < 1 \\ &\alpha_2(1+\eta)\sqrt{1-\beta_2\left(\beta_a\gamma_a(1+\gamma_a\beta_a^{-1}/2)/(1+\eta)\right)^2} \le S_{t0} \\ &\alpha_1(1+2\gamma_a)/(1+\eta) \le \gamma_a^2 < 1 \\ &b_a \le \alpha_0(1+\eta) \end{aligned}. \tag{35}$$

The coefficient α_η of the stability inequality, the first term in (35), includes the peak $|\partial\mathbf{P}_a(f_{\partial a})|$ of the neglected dynamics; α_1, β_2 are ratios between drag spectral density and requirements, and α_0, α_2 are spectral bounds. Inequality (35), if feasible, can be shown to converge, starting from $\eta = 0$. More specifically (i) the first inequality, providing η, establishes whether the stability robustness, expressed by $\eta_{\max} < 1$, is feasible; (ii) the second inequality provides an upper bound to thruster noise spectral density S_{t0} defined in (13); (iii) the third inequality provides a lower bound to γ_a whereas the upper bound is given by the first inequality; (iv) the final inequality provides a bound to the accelerometer bias b_a.

5 Simulated results

Simulated results derive from a fine GOCE simulator. The simulator includes fine models of gravity anomalies, of the Earth's magnetic field and of thermosphere density: stochastic extrapolation has been applied to match a simulation step less than $T = 0.1$ s. Drag forces and torques are computed from simplified satellite geometry. Simulated results refer to worst-case mission conditions and to the sequence of the phases in Table 2, from fine pointing and calibration during commissioning to the science phase, which latter has being treated in [9].

The performance of position drag-free control is shown in the time and frequency domain. During pointing mode, as accelerometers are OFF, $l_a = 0$, drag-free control (29) is silent except for setting the along-track thrust equal to mean drag, so as to maintain orbit. Drag-free control starts as soon as the accelerometers are ON, $l_a = 1$, at $t = 68.5$ ks, during the calibration phase, $l_g = 0$, lasting until $t = 79$ ks, when the bias of the angular accelerations is under calibration. Figure 1 shows the along-track and out-of-plane residual accelerations. Oscillations correspond to orbital periods. Only the along-track component is forced to zero from DC to mid frequency. Lateral accelerations are not forced to zero either in fine-pointing or in the science mode in order to save propellant and limit the thruster peak [9]: they are forced to zero only at mid frequencies.

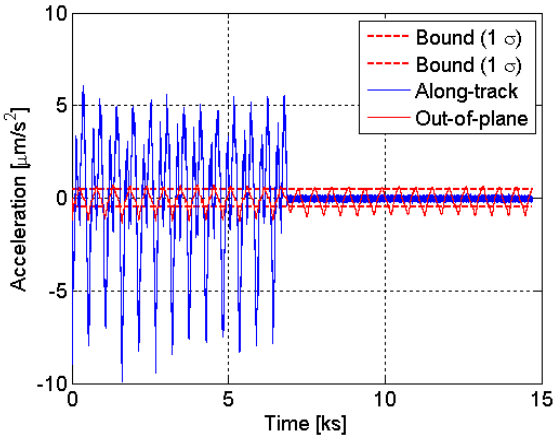

Figure 1 Time history of the center-of-mass non-gravitational acceleration.

Figure 2 compares along-track non-gravitational acceleration to the target bound during pointing and science modes. The low-frequency jump in the science mode is due to CoM accelerometer bias, which is not calibrated. As expected from the design, the science mode spectral density shows a margin.

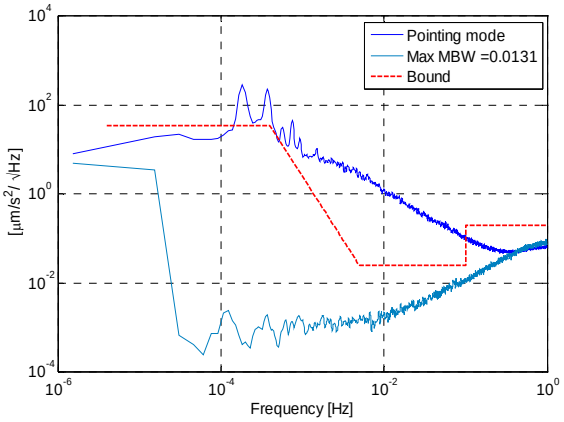

Figure 2 Spectral density of the along-track acceleration (pointing and science modes, and target bound).

A summary of fine-pointing and science mode performance is given in Table 3, but is limited to CoM acceleration. The performance of each axis is compared to mid-frequency requirements.

Table 3. Simulated performance within GOCE mid frequency

Variable	Mode	Unit	Along-track	Out-of-plane	Radial	Science bound
a	Pointing	$\left(\mu m/s^2\right)/\sqrt{Hz}$	3.200	0.114	0.095	
	Science	$\left(\mu m/s^2\right)/\sqrt{Hz}$	0.013	0.010	0.007	0.025

Figure 3 shows the angular accelerations estimated from the star tracker measurements, during pointing and science modes. They join at $t = 79$ ks through the large bias estimated during the calibration phase by the drag-free state-predictor corresponding to subset 2 in Table 2. During pointing and calibration phases, the perturbing torques (Section 2.3) are estimated by the attitude state-predictor defined by subset 1 in Table 2: they are shown in Figure 3 for $t < 79$ ks, in angular acceleration units. The estimation time has been made longer than 10 ks for plotting purposes. In the science mode the opposite occurs, as the attitude state-predictor (subset 1) only estimates the weak accelerometer drift which is obscured in Figure 3 by accelerometer bias. Perturbing torques are instead estimated from the drag-free predictor (subset 2) and cancelled by the control law (29).

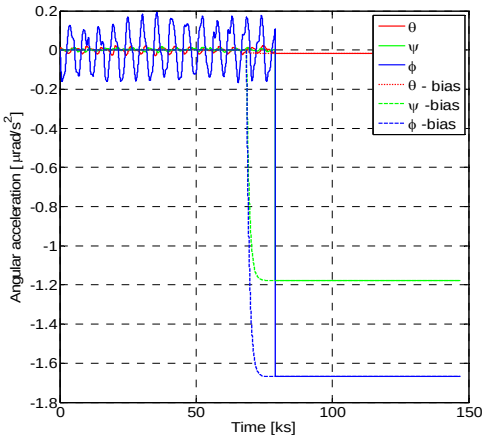

Figure 3 Angular accelerations estimated by attitude predictor in the pointing (left) and science modes (right).

Figure 4 shows the residual angular rate and illustrates the difference in performance between pointing and science modes. The pointing mode is dominated by star-tracker noise, which can be filtered out in the science mode so as to meet attitude and angular rate requirements in the mission band $\mathcal{F}_1$. The same noise cannot be adequately filtered out in the pointing mode so as to make available a wider BW than in the science mode, and thus to cancel perturbing torques in the absence of drag-free control.

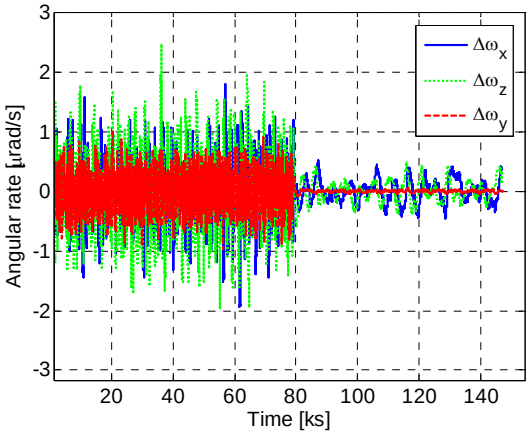

Figure 4 Residual angular rate in the pointing (left) and science modes (right).

6 Conclusions

The paper outlines Embedded Model and noise design for drag-free and attitude control, that can combine position/attitude and accelerometer measurements in a suite of control modes. Noise design selects the necessary and sufficient feedback channels for updating disturbance to be rejected in real-time. The resulting models and state predictors are rather generic, and apply to future drag-free missions requiring satellite formation. Models and predictors constitute the formal image of the control code and enable a smooth switching between control modes, by means of appropriate Boolean variables. Feedback gains are tuned by means of eigenvalue assignment, respecting performance and robust stability. Simulated results are outlined showing performance under

different modes which are typical of drag-free missions like GOCE. Soon after the launch in Spring 2009, GOCE entered the early stages of the pointing mode, prior to commissioning and science mode.

7 Acknowledgements

Part of the work of one of the authors was done under a grant of Thales Alenia Space Italia, Turin, Italy, prime contractor of the GOCE satellite. The author is indebted to the reviewers for their helpful suggestions.

8 References

[1] E. Canuto and L. Massotti "All-propulsion design of the drag-free and attitude control of the European satellite GOCE", *Acta Astronautica*, 65, 2009, p. 325-344.

[2] L. Vaillon, J. Borde, T. Duhamel and P. Damilano "Drag-free control systems and technologies", *Space Technol.,* 16 (5/6), 1996, p. 245-254.

[3] W. Fichter, A. Schleicher, L. Szerdahelyi, S. Theil and P. Airey "Drag-free control system for frame dragging measurements based on cold atom interferometry", *Acta Astronautica,* 57, 2005, p. 788-799.

[4] B. Ziegler and M. Blanke "Drag-free motion control of satellite for high-precision gravity field mapping" in *Proc. 2002 IEEE Int. CCA,* Glasgow (Scotland, UK), 2002, p. 292-297.

[5] E. Canuto, "Embedded Model Control: outline of the theory", *ISA Trans.,* 46 (3), 2007, p. 363-377.

[6] D.J. Scheeres "The restricted Hill four-body problem with applications to the Earth-Moon-Sun system", *Celestial Mechanics and Dynamical Astronomy,* 70, 1998, p. 75-98.

[7] J. C. Doyle, B. Francis and A. Tannenbaum *Feedback control theory,* Macmillan Pu. Co., New York, 1992.

[8] E. J. Lefferts and F.L. Markley "Kalman filtering for spacecraft attitude estimation", *Journal of Guidance, Control and Dynamics,* 5 (5), 1982, p. 417-429.

[9] E. Canuto "Drag-free and attitude control for the GOCE satellite", *Automatica,* 40 (7), 2008, p. 1766-1780.

[10] W. M. Wonham *Linear multivariable control: a geometric approach,* Springer, New York, 1985.

[11] K. Zhou and J.C. Doyle *Essentials of robust control,* Prentice-Hall Inc., Upper Saddle River (NJ), 1998.

[12] J. Ospina and E. Canuto "Embedded Model Control and the error loop", *Proc. 8th Int. FLINS Conf.,* World Scientific Pu., Singapore, 2008, p. 975-980.